Lithosphere

Research Article

Fracture Propagation Behavior of Bedding Shale in the Process of Multistage Cluster Fracturing considering the Intercluster Stress Interference

Qingqing Zhang [iD],[1,2] **Huanqiang Yang** [iD],[1,2] **Yang Liu,**[3] **Dong Xiong,**[4] **and Yuntao Mei**[1,2]

[1]*Department of Petroleum Engineering, Yangtze University, Wuhan 430100, China*
[2]*Key Laboratory of Drilling and Production Engineering for Oil and Gas, Wuhan 430100, China*
[3]*Engineering Technology Research Institute of PetroChina Xinjiang Oilfield Company, Karamay 834000, China*
[4]*College of Petroleum Engineering, China University of Petroleum-Beijing, Beijing 102249, China*

Correspondence should be addressed to Huanqiang Yang; yanghuanqiang@yangtzeu.edu.cn

Staged multicluster fracturing in horizontal wells is the key technology for forming complex fractures in shale reservoirs. The existence of shale bedding plays a conspicuous role for the propagation path of hydraulic fractures, affecting the propagation of the fracture height direction prominently. A 3D finite element model containing three clusters signed as side clusters and middle cluster was established based on the cohesive zone model and the dynamic distribution mechanism of interfracture flow. And the correctness of the model was verified by literature comparison. Some factors including cluster spacing, horizontal stress difference, shale bedding strength, perforation density, injection rate, and viscosity of fracturing fluid which influenced fracture propagation behavior of bedding shale were simulated. The results indicate that the stress interference of the middle cluster by the clusters on both sides will be prominently obvious when the cluster spacing is less than 10 m. Multiclusters will penetrate across the shale bedding when the horizontal stress difference is more than 4 MP, which will conspicuously reduce the activated probability of discontinuities and the complexity of fracture geometry. In correspondence with increase of horizontal stress difference, the interference between clusters also increases prominently, which will conspicuously decrease the propagation of the middle cluster. In order to comprehensively equalize the length of multiclusters, the inhibition of intercluster stress interference on the middle cluster propagation can be counteracted by improving pressure drop in perforation. The high injection rate and viscosity of fracturing fluid will contribute to the shale bedding shear slip increasingly, which is conducive to the formation of complex fractures in areas with well-developed bedding. The study has a certain guiding significance for the operation parameter design of multicluster fracturing in bedded shale.

1. Introduction

Shale reservoirs have the poor properties with low porosity and low permeability. Horizontal well-staged fracturing is an effective technology to stimulate the reservoirs. Forming large-scale complex fracture networks by staged multicluster fracturing is the key to effectively developing the shale reservoirs [1]. There are many beddings inside the shale, with uneven thickness and well-developed interlayer weak structural plane, which are not conducive to the propagation of hydraulic fractures in the direction of height. Many scholars have done numerous researches on the propagation law of fractures at natural fractures [2]. Considering the existence of natural fractures, Khoei et al. [3] adopted the numerical simulation method to research the multicluster fracture propagation problem. And Zhang et al. [4], Tan et al. [5], Zhang et al. [6], and Bilgen et al. [7] studied the influence of geological conditions and construction parameters on the propagation law of fractures by indoor experiments. However, physical model experiments are usually conducted

with pseudostress conditions and the fracture distributions are described difficultly. With the development of computer technology, numerical simulation has become an important means to study the fracturing process [8].

Some numerical simulation methods, like finite element method (FEM), boundary element method (BEM), extended finite element method (XFEM), displacement discontinuity method (DDM), and discrete element method (DEM), are usually employed to study the fracture propagation. Li et al. [9] and Sukumar et al. [10] investigated dynamic distribution of injection flow rule of fracture spacing optimization in the process of multistage fracturing by XFEM. Based on laboratory mechanical experiments, Zhou et al. [11, 12] framed a 3D model of hydraulic fracture propagation by DEM, and vertical stress difference on fracture propagation was researched. Liu et al. [13] founded a mathematical model of shale gas volume fracturing bedding fracture propagation by a pseudo-three-dimensional (P3D) method, discussing the effect of bedding planes on the geometric parameters of fractures. Xu et al. [14] and Wu and Olson [15] established an in situ stress field model under the interference model of staged multicluster fracturing by DDM, and the mechanism of natural fracture opening or shearing rupture to form complex fracture networks was analyzed. However, it is difficult for XFEM to simulate the propagation of three-dimensional fractures because it cannot set pore pressure, and the DEM has low computational accuracy. Wang et al. [16] created a 3D fracture propagation model considering the plane strength, perforation position, and pumping rate by embedding a global cohesive element; it was found that increasing the pumping rate will increase the fracture height and achieve the purpose of cross-layer stimulation. Some factors including principal stress, distribution, and direction of natural fractures were studied by the cohesive method, and the result shows that they have a significant effect on fracture propagation and the induction of complex fracture networks [17, 18]. Using cohesive element to set up multilayer hydraulic fracture propagation model, the vertical propagation law of a single fracture at the shale bedding was studied by Sun et al. [19], Suo et al. [20], and Xiong et al. [21]. Without considering the dynamic distribution of fluid, a new computational version of the particle-based model is established based on the Xsite. Liu et al. [22] researched the fracture propagation in multicluster fracturing with three natural fractures, and three fracturing sequences including simultaneous fracturing, bilateral fracturing, and sequential fracturing were simulated. It is found that the cluster spacing and in situ stress differences have significant effects on the length and morphology of hydraulic fractures. The influence of the perforation scheme on the simultaneous propagation of multifractures was discussed. Li et al. [23] established the finite element calculation model of fracture propagation in horizontal staged multicluster fracturing. Varying 2~3 perforation density will effectively balance the stress interference between fractures [24]. Zhao et al. [25] established a numerical model for the dynamic propagation of multistage and multicluster fractures. The effects of perforation hole friction, cluster spacing, viscosity, and rock elastic modulus on multifracture propagation were

studied. The above studies did not consider the form of fracture propagation when the shale bedding was included.

Based on the cohesive zone model and the dynamic distribution mechanism of interfracture flow, a 3D finite element model of multicluster fracture propagation in shale bedding was established using the cohesive element, Fluid Pipe Element (FP3D2 element), and Fluid Pipe Connector Element (FPC3D2 element). And the propagation behavior of multicluster fractures in the bedding plane considering intercluster stress interference was revealed.

This paper is organized as follows. First, a theoretical model was established in Chapter 2. Then, a numerical simulation model was established, and the correctness of the model was verified by literature comparison in Chapter 3. In addition, some factors including cluster spacing, horizontal stress difference, shale bedding strength, perforation parameter, injection rate, and viscosity of fracturing fluid which influenced fracture propagation behavior of bedding shale were simulated in Chapter 4. Finally, according to the research findings, some instructional proposals to field fracturing practice are given in Chapter 5.

2. Theoretical Model

2.1. Flow-Solid Coupling Equation. The fracturing process is mechanically divided into three flow fields in mechanics: the fluid flow field, the rock stress field, and the pore seepage field. In segmented multicluster fracturing, interfracture stress interference is generated with the changes of the three flow fields [26]. The sustained pumping of fracturing fluid results in the continuous increase of fluid pressure in the fracture and rock pore pressure. Rock stress state often leads to the change of porosity and fluid flow state, which ultimately brings about the alteration of reservoir pore pressure. Thus, the fluid seepage and rock deformation are mutually regulated and influenced during the process of fluid injection in hydraulic fracturing, which is referred to as rock seepage-stress coupling.

Effective stress principle for the reservoir matrix is [26]

$$\bar{\sigma} = \sigma + mp_w, \tag{1}$$

where $\bar{\sigma}$ is the effective stress of reservoir matrix, Pa; σ is the total stress of reservoir, Pa; P_w is the pore pressure, Pa; and m is equal to $[1, 1, 1, 0, 0, 0]^\tau$.

Rock balance equation for fractured reservoir [27]:

$$\int_V (\bar{\sigma} - mp_w) \delta\varepsilon dV = \int_S t\delta v dS + \int_V f\delta v dV, \tag{2}$$

where $\delta\varepsilon$ is the virtual strain rate of reservoir matrix, s^{-1}; t is the unit surface load, N/m^2; δv is the virtual velocity of reservoir matrix, m/s; f is the physical load, N/m^3; dS is the action area of surface load, m^2; dV is the calculation of unit volume, m^3.

According to the conservation of mass, the fluid continuity equation is

$$\int_V \delta v \frac{1}{J} \frac{d}{dt}(J\rho_w n_w)dV + \int_V \delta v \frac{\partial}{\partial x}(\rho_w n_w v_w)dV = 0, \quad (3)$$

where J is the volume change rate of reservoir pores, dimensionless; n_w is the ratio of liquid volume to total reservoir volume in pores, dimensionless; ρ_w is the reservoir fluid density, kg/m^3; x is the direction vector of fluid flow, m; dt is the time step, s; v_w is the velocity of fluid flow, m/s.

The calculation formula of pore fluid flow velocity is [28]

$$v_w = -\frac{a\mu}{n_w \rho_w g} K \left(\frac{\partial p_w}{\partial x} - \rho_w g\right), \quad (4)$$

where a is the unit conversion constant; g is the gravity acceleration, m/s^2; μ is the pore liquid viscosity, Pa·s; K is the dynamic permeability of the reservoir, mD; ∂p_w is the flow velocity of reservoir fluid, m/s.

Throughout the hydraulic fracturing process, the porosity φ and permeability k of the reservoir change with the pore volume, and the two parameters are updated in real time with the calculation process. The pore pressure and stress in the reservoir are coupled to each other; the changes in pore pressure and effective stress will have an effect on φ and k. The dynamic equation for fluid-solid coupling is

$$\begin{cases} \varphi = \dfrac{\varphi_0 - \varepsilon_v}{1 - \varepsilon_v}, \\ k = k_0 \dfrac{1}{1 - \varepsilon_v} \left\{1 - \dfrac{\varepsilon_v}{\varphi_0}\right\}, \end{cases} \quad (5)$$

where φ is the porosity of reservoir rock, dimensionless; k is the permeability of reservoir rock, dimensionless; φ_0 is the initial porosity of reservoir rock, dimensionless; k_0 is the initial permeability of reservoir rock, μm; ε_v is the change rate of the pore volume.

2.2. Friction Pressure Drop in Perforation. From Figure 1, the fluid flows through the wellbore and then to each fracture cluster with uncertain flow rate. And the flow of fluid in the wellbore meets Kirchhoff's first and second laws [29].

Ignoring the wellbore effect, the total injection rate is the sum of the injection rates inside each cluster.

$$Q_T = \sum_{i=1}^{N} Q_i, \quad (6)$$

where Q_T is the total injection rate, m^3/s; Q_i is the injection rate for i cluster, m^3/s.

According to the continuity of wellbore pressure, the bottom hole pressure is equal to the sum of the friction pressure drop in the perforation and wellbore and the pressure in the first unit of each fracture branch.
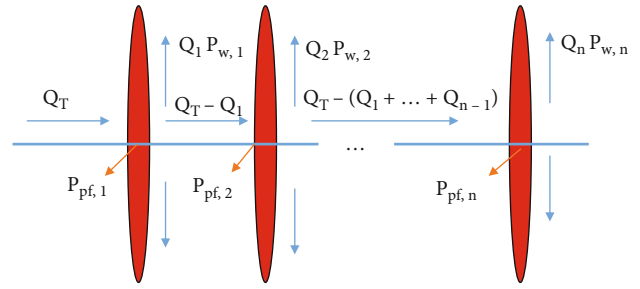
$$P_0 = P_{pf,i} + P_{w,i} + P_{cf,i}, \quad (7)$$

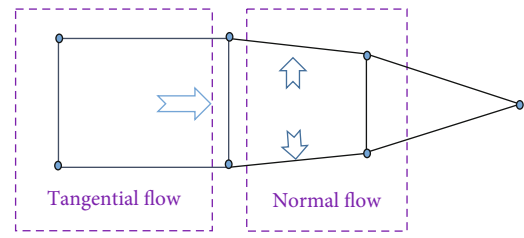FIGURE 1: Flow and pressure distribution of multicluster propagation.

FIGURE 2: Schematic diagram of cohesive fluid flow.

where P_0 is the fluid pressure at the good root, Pa; $p_{pf,i}$ is the perforation friction, Pa; $p_{w,i}$ is the fracture first cluster pressure, Pa; $p_{cf,i}$ is the wellbore friction, Pa.

$p_{pf,i}$ can be calculated by Bernoulli equation [30].

$$P_{pf,i} = \frac{0.807\rho_s}{n_{p,i}^2 d_{p,i}^4 K_d^2} Q_i^2, \quad (8)$$

where K_d is the dimensionless coefficient, which takes 0.56 and 0.89, respectively, before and after perforation; ρ_s is the fracturing fluid density, kg/m^3; $n_{p,i}$ is the number of perforations; $d_{p,i}$ is the perforation diameter, m.

Pressure drop in each fracture of the wellbore can be gained with the utilization of

$$\begin{cases} P_{cf,i} = C_{cf} \sum_{j=1}^{i} (x_j - x_{j-1}) Q_{w,j}, \\ Q_{w,j} = Q_T - \sum_{k=1}^{j-1} Q_k(j-1), \\ Q_{w,j} = Q_T(j=1), \\ C_{cf} = \dfrac{128u}{\pi D^4}, \end{cases} \quad (9)$$

where C_{cf} is the frictional coefficient, μ; x_j is the distance from j fracture to wellbore bottom, m; $Q_{w,j}$ is the residual fluid flow for j fracture, m^3/s; D is the bore diameter in fracturing section, m.

2.3. Fluid Flow Equation. The driving force, generated by fluid pressure acting on the fracture surface, will promote the fracture to open and propagate forward. The cohesive
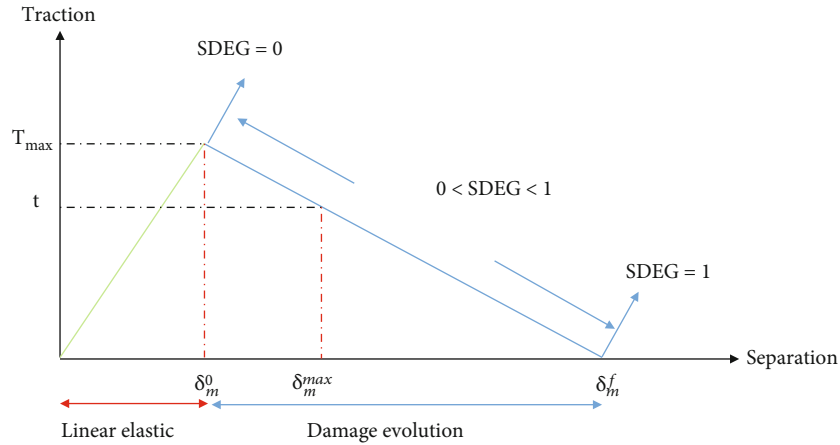
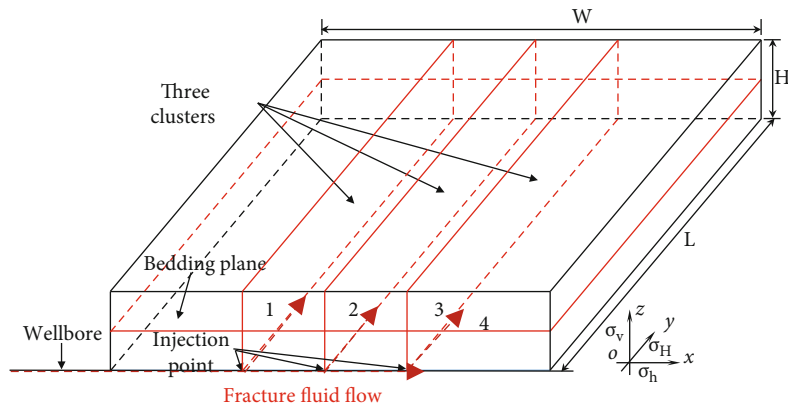FIGURE 3: Bilinear traction-separation criterion.

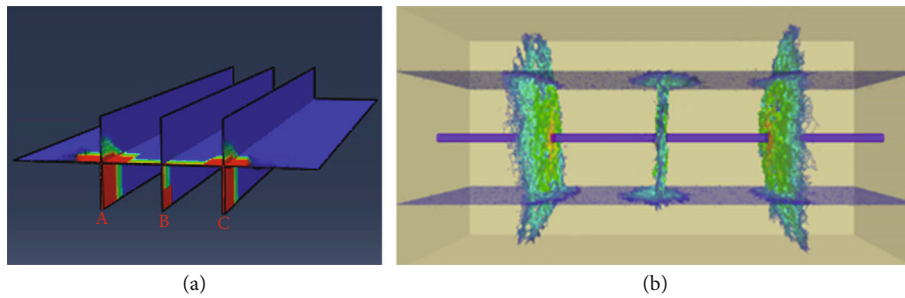

FIGURE 4: The 3D geometric model for bedded shale.

FIGURE 5: The results of numerical simulation. (a) The result of cohesive element model. (b) Liu et al. [22].

zone model is usually employed to simulate the fracture propagation due to the fact that it has the advantage to describe the cross-propagation of fractures and bedding plane [21]. And the fluid in the fracture of the cohesive element can be divided into tangential and normal flows, where some of them will filter through the fracture surface into the formation pores. As is shown in Figure 2, the fracturing fluid is regarded as an incompressible Newtonian one, and the normal and tangential flows are perpendicular and parallel to the fracture surface, respectively.

TABLE 1: Comparison of the fracture height between numerical model and literature.

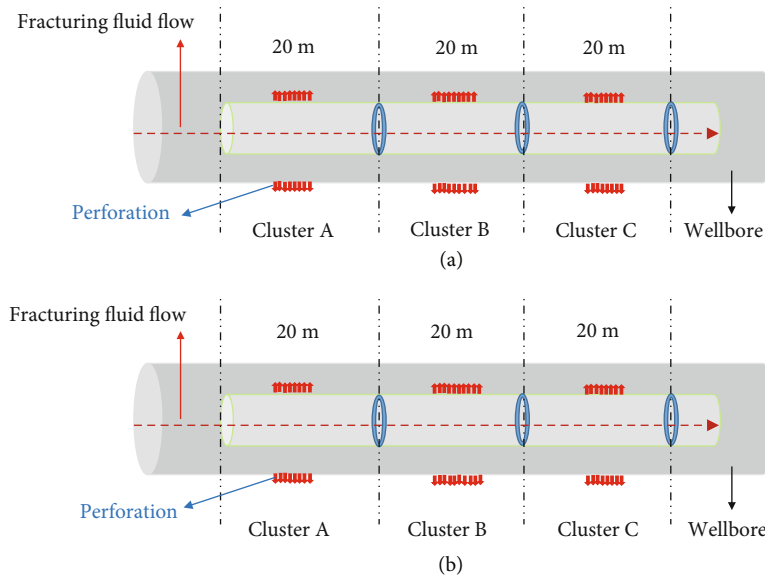| Result sources	Half fracture height (m)		
	Cluster A	Cluster B	Cluster C
Cohesive element model	5.0	4.0	5.0
Liu et al. [22]	4.9	4.0	4.9

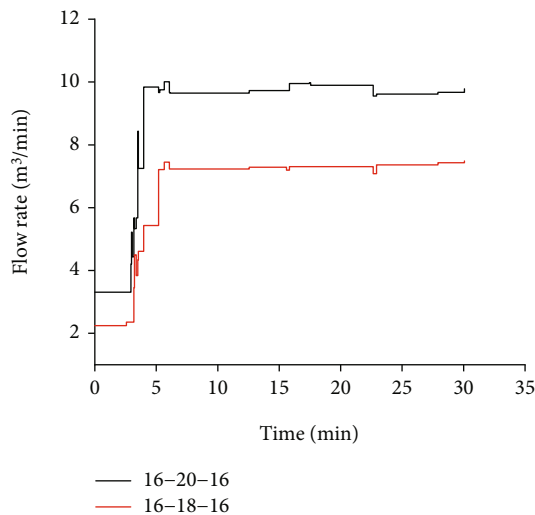FIGURE 6: Perforation density schematic diagram: (a) 16-18-16 and (b) 16-20-16.

FIGURE 7: Flow distribution of each middle cluster under different perforation density.

TABLE 2: Model parameters.

Parameters	Value
Shale matrix	
Young's modulus (Pa)	12×10^9
Tensile strength (Pa)	3×10^6
Poisson's ratio	0.2
Permeability (m/s)	1×10^{-7}
Shale bedding	
Permeability (m/s)	1×10^{-7}
Strength (Pa)	2×10^6
Stiffness (Pa)	12×10^9
Fracturing construction parameters	
Time (s)	2000
Cluster spacing (m)	20
Injection rate (m^3/min)	12
Viscosity (mPa·s)	3
Cluster number	3
Perforation number per cluster (hole)	16
Hole diameter (m)	0.012

The shale bedding plane will be directly penetrated by hydraulic fracture without any shear slip when its strength is more than the fluid pressure in the fracture tip, while the shear slip will be generated on the contrary. The tangential flow equation [31, 32] and mass conservation equation [32] are as follows:

$$q = -\frac{w^3}{12\mu}\nabla p_f, \tag{10}$$

$$\frac{\partial w}{\partial t} + \nabla \cdot q + q_t + q_b = Q(t)\delta(x), \tag{11}$$

where ∇p_f is the fluid pressure gradient along with fracture, Pa; q is each fracture tangential flow and equal to the average tangential velocity multiplied by the fracture opening, m^3/s;

w is the fracture width, m; μ is the fracturing fluid viscosity, mPa·s; $\delta(x)$ is the Dirac function; $Q(t)$ is the fluid injection rate at time t, m^3/s.

Normal flow of fracturing fluid on the upper and lower surfaces of the cohesive element can be expressed as follows [33]:

$$\begin{cases} q_t = q_t\left(p_f - p_t\right), \\ q_b = c_b\left(p_f - p_b\right), \end{cases} \tag{12}$$
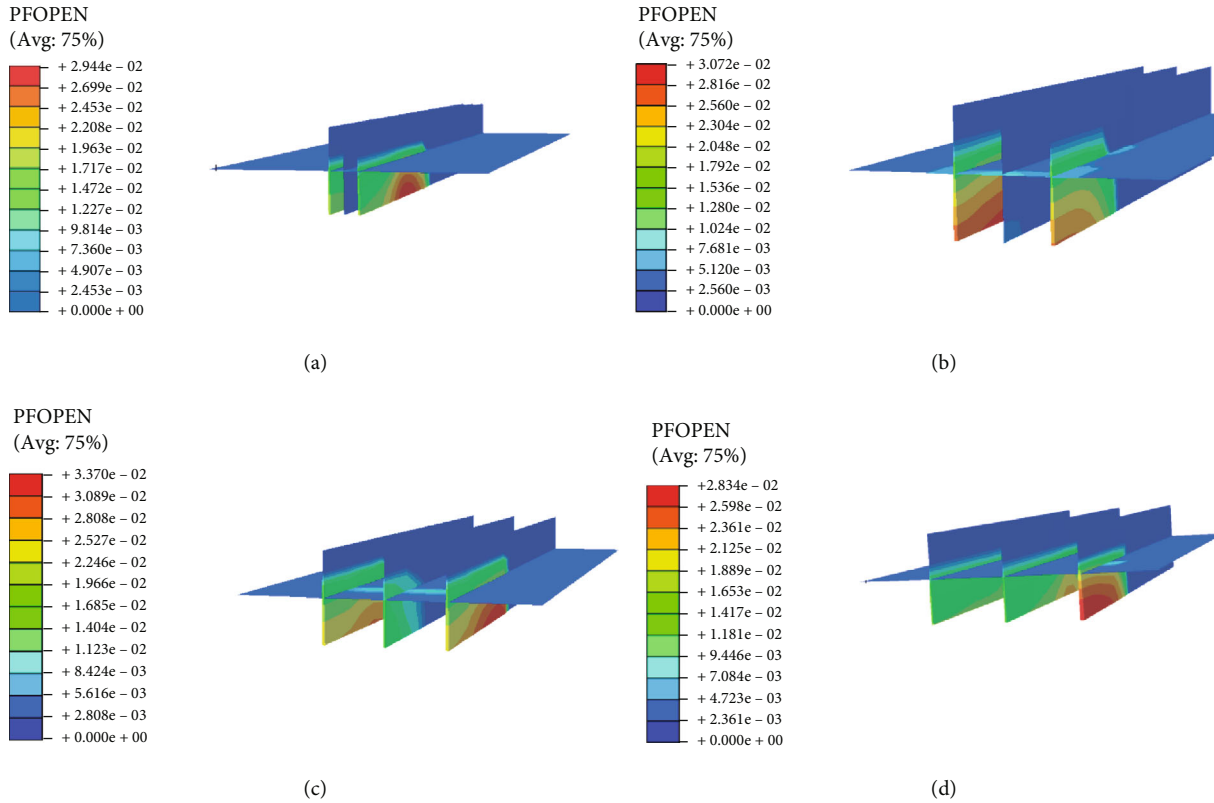
(a)

(b)

(c)

(d)

FIGURE 8: The simulation results of the fractures under different cluster spacing: (a) 10 m, (b) 15 m, (c) 20 m, and (d) 25 m.

where q_t, q_b are the fracturing fluid flow along the upper and lower surfaces, m^3/s; c_t, c_b are the filtration coefficients of fluid on the upper and lower surfaces, dimensionless; p_i is the fluid pressure in the middle of the fracture element, MPa; p_t, p_b are the pore pressure of the fluid on the upper and lower surfaces of the fracture, MPa.

Equation (13) can be obtained by combining with equations (10), (12), and (11).

$$\frac{\partial w}{\partial t} + c_t\left(p_f - p_t\right) + c_b\left(p_f - p_b\right) = \frac{1}{12\mu}\nabla \cdot \left(w^2\nabla p_f\right) + Q(t)\delta(x). \tag{13}$$

The pressure drop gradient satisfies equation (14) on the assumption that the fracturing fluid between two parallel plates is laminar flow.

$$\frac{dp}{dx} = -\frac{12\mu q}{h_f w^3}, \tag{14}$$

where h_f is the fracture height, m.

The equation for the pressure drop at the inner surface of the fracture is as follows:

$$\begin{cases} P = -\dfrac{12\mu qx}{h_f w_0^3} + P_0, & P > \prod, \\ P = \prod, & P \leq \prod, \end{cases} \tag{15}$$

where Π is the permeation pressure, MPa; w_0 is the maximum fracture width, m.

2.4. Fracture Initiation and Propagation Criteria. The cohesive element adapting the traction-separation criterion of element stiffness degradation is employed to simulate the initiation and propagation of fractures in bedded shale. In Figure 3, the loading failure process considered as linear elasticity in the traction-separation criterion can be divided into $0 < \delta \leq \delta_0$, $\delta_0 < \delta \leq \delta_f$, and $\delta > \delta_f$ three stages. The first stage suggests that traction gradually reaches the peak T_{max} and SDEG = 0 at this point, and the cohesive element begins to be damaged. Then, the traction reduces to 0 and the critical value SDEG = 1 when the opening displacement cannot reach. Finally, the cohesive element is destroyed completely and filled with fracturing fluid, so as to initiate hydraulic fracture.

The constitutive relation of the bilinear traction-separation criterion is [34]

$$T = \begin{cases} K_0\delta, & 0 \leq \delta \leq \delta_0, \\ (1 - \text{SDEG})K_0\delta, & \delta_0 \leq \delta \leq \delta_f, \\ 0, & \delta \geq \delta_f, \end{cases} \tag{16}$$

where K_0 is the initial stiffness of cohesive element; δ is the separation quantity of cohesive element in the loading process; SDEG is the overall damage factor of material.
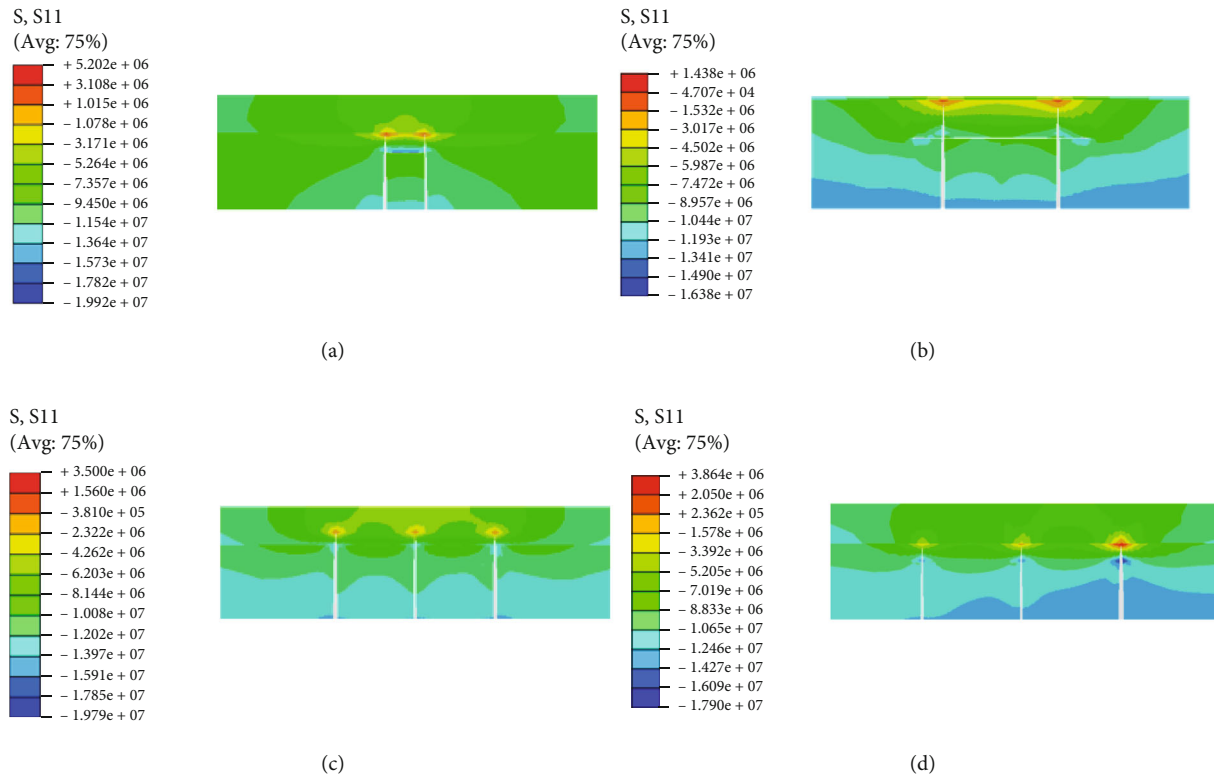
FIGURE 9: The cloud diagram for the minimum horizontal stress of the fractures under different cluster spacing: (a) 10 m, (b) 15 m, (c) 20 m, and (d) 25 m.
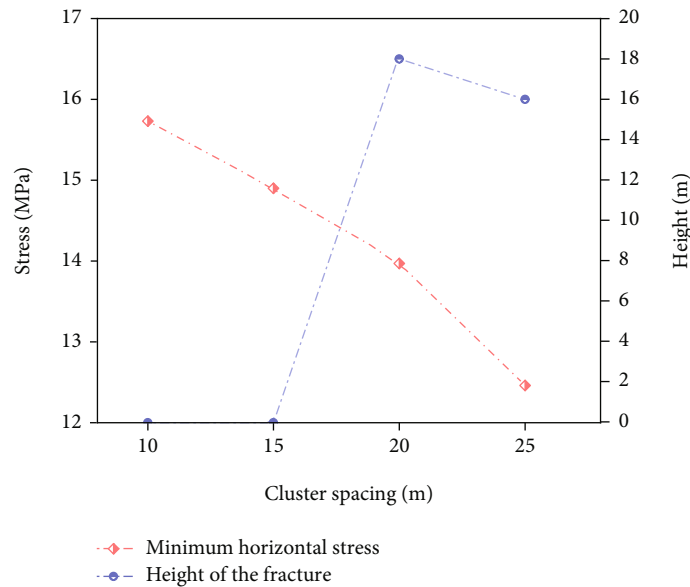

FIGURE 10: The results of minimum horizontal stress and height for the middle fracture.

The minimum secondary stress criterion is used as the criterion for simulating the initiation of the shear slip in bedding plane; that is, when the sum of squares of stress is 1, the initial fracture of rock begins to occur [35].

The hydraulic fracture will be initiated when the stresses satisfy the minimum secondary stress criterion shown in equation (17), so does the initiation of the shear slip for bedding plane [35].

$$\left\{\frac{\langle T^n \rangle}{T_0^n}\right\}^2 + \left\{\frac{(T^s)}{T_0^s}\right\}^2 + \left\{\frac{(T^t)}{T_0^t}\right\}^2 = 1, \tag{17}$$

PFOPEN
(Avg: 75%)

+2.216e − 02
+2.031e − 02
+1.847e − 02
+1.662e − 02
+1.477e − 02
+1.293e − 02
+1.108e − 02
+9.234e − 03
+7.387e − 03
+5.540e − 03
+3.694e − 03
+1.847e − 03
+0.000e + 00

(a)

PFOPEN
(Avg: 75%)

+3.370e − 02
+3.089e − 02
+2.808e − 02
+2.527e − 02
+2.246e − 02
+1.966e − 02
+1.685e − 02
+1.404e − 02
+1.123e − 02
+8.424e − 03
+5.616e − 03
+2.808e − 03
+0.000e + 00

(b)

PFOPEN
(Avg: 75%)

+3.602e − 02
+3.302e − 02
+3.002e − 02
+2.702e − 02
+2.402e − 02
+2.101e − 02
+1.801e − 02
+1.501e − 02
+1.201e − 02
+9.006e − 03
+6.004e − 03
+3.002e − 03
+0.000e + 00

(c)

PFOPEN
(Avg: 75%)

+3.114e − 02
+2.855e − 02
+2.595e − 02
+2.336e − 02
+2.076e − 02
+1.817e − 02
+1.557e − 02
+1.298e − 02
+1.038e − 02
+7.786e − 03
+5.191e − 03
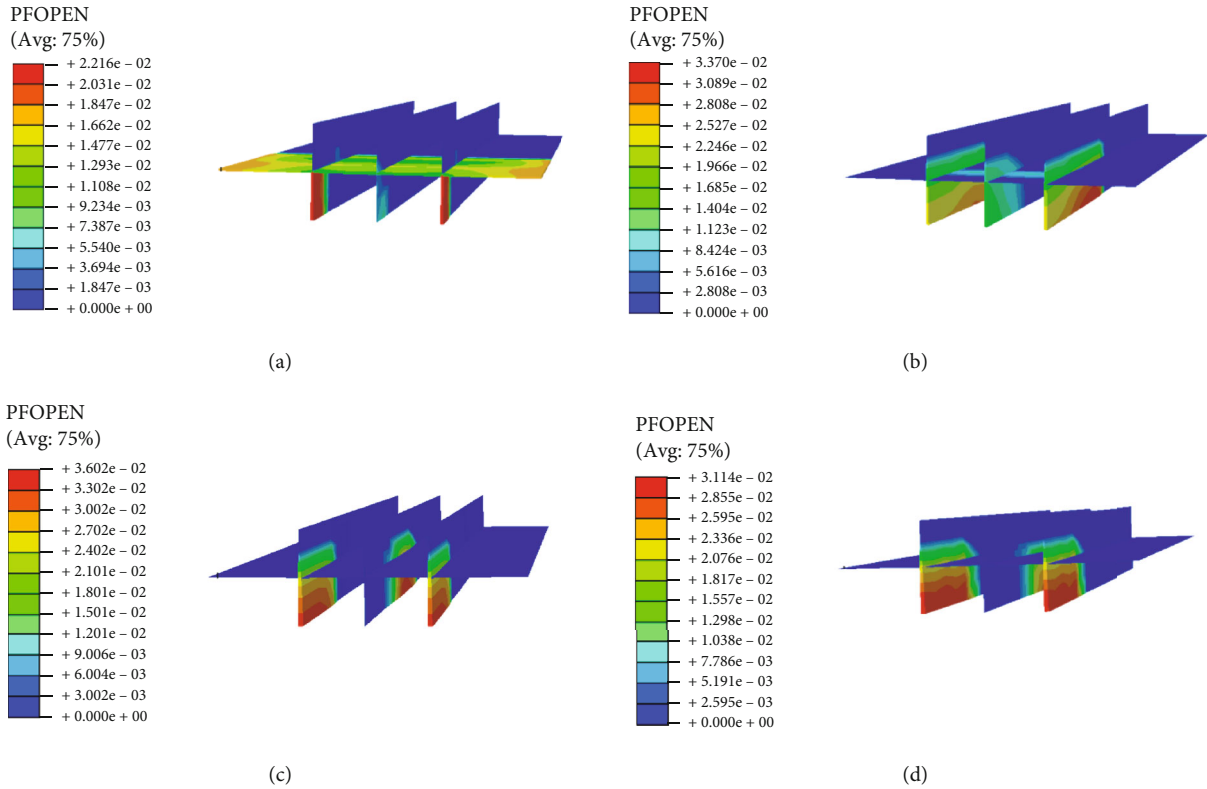+2.595e − 03
+0.000e + 00

(d)

FIGURE 11: The propagation behavior of the fractures under different horizontal stress differences: (a) 0 MPa, (b) 2 MPa, (c) 4 MPa, and (d) 6 MPa.

where T^n is the normal stress on the cohesive element; T^s, T^t are the shear stress on the cohesive element; $T_0{}^n$, $T_0{}^t$, and $T_0{}^s$ are the nominal stress peak perpendicular to the plane and two mutually perpendicular shear directions on the plane, respectively.

The linear damage evolution can be calculated by

$$\mathrm{SDEG} = \frac{\delta_m^f \left(\delta_{\mathrm{m}}^{\max} - \delta_m^0 \right)}{\delta_{\mathrm{m}}^{\max} \left(\delta_m^f - \delta_m^0 \right)}, \qquad (18)$$

where $\delta_m{}^f$ is the displacement when the cohesive element is completely destroyed, m; $\delta_m{}^{\max}$ is the maximum displacement in the failure process of the cohesive element, m; $\delta_m{}^0$ is the displacement at the beginning of damage of the cohesive element, m.

3. Model Establishment and Verification

3.1. Model Establishment. Based on the engineering background of the Weiyuan area in Sichuan Basin [22], a 3D geometric model for bedded shale is established with the size of $L \times W \times H = 200\,\mathrm{m} \times 100\,\mathrm{m} \times 30\,\mathrm{m}$, as shown in Figure 4. One bedding plane and three cluster planes are considered in the model, which are represented by the cohesive element. And the fracturing fluid is assumed to be injected into each fracture simultaneously from the injection point with a constant rate, and the red arrow imaginary line in Figure 4 is the

TABLE 3: Propagation behavior of the fractures at the shale bedding plane.

Horizontal stress differences (MPa)	Open the bedding plane	Penetrate the shale bedding
0	Yes	No
2	Yes	Yes
4	No	Yes
6	No	Yes

flow direction of the fracturing fluid. The meshing is introduced into the model to improve the accuracy and convergence of calculation, while it is seeded densely near the cohesive elements.

3.2. Model Validation. Take the same parameters of numerical model in Liu et al. [22] to simulate the propagation of multicluster hydraulic fractures without considering the distribution mechanism of each cluster flow, in which the results are shown in Figure 5 and Table 1.

It can be seen from Figures 5(a) and 5(b) that the hydraulic fractures induce the shear slip of the bedding plane. However, the fractures on both sides penetrate through the bedding plane, neither does the one in the middle. And the results of the half fracture height of numerical simulation shown in Table 1 are almost the same. Therefore, the cohesive element model has the sufficient precision and
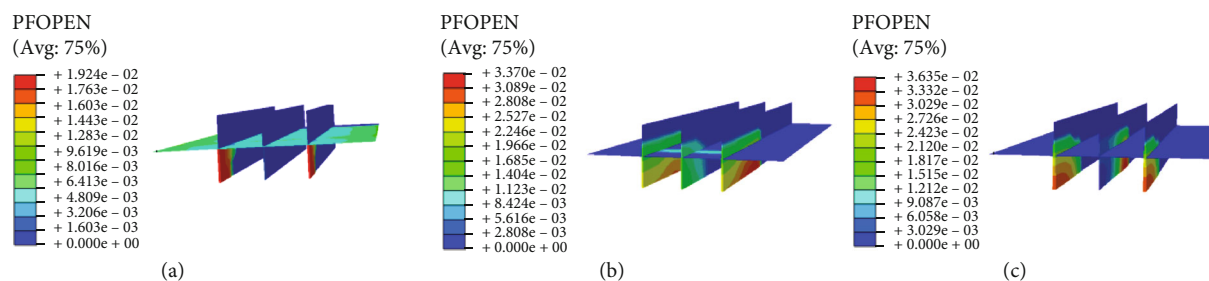
FIGURE 12: The propagation behavior of the fractures in the bedding plane under different shale bedding strength: (a) 0.5 MPa, (b) 2 MPa, and (c) 4 MPa.

accuracy to simulate the propagation of multicluster fractures in bedded shale.

3.3. Fracture Fluid Flow Distribution Regularity. There are several significant factors playing a highly important role on the flow distribution of multiclusters, including cluster spacing, wellbore diameter, and perforation density. By keeping the values of cluster spacing and pump rate at 20 m and 12 m^3/min and the wellbore diameter unchanged, the perforation density of 16-18-16 and 16-20-16 in Figure 6 is set, respectively, to research the influence of it on the flow distribution, in which the results are illustrated in Figure 6.

The results show that the flow rate of the middle cluster is, respectively, 9.6 m^3/min and 7.3 m^3/min represented by the black and red curve in Figure 7, suggesting the perforation density has an obvious influence on the flow distribution. In other words, the flow rate inside the fracture will increase with the improvement of perforation density.

4. Results and Discussion

The parameters for the bedded shale gained from the Weiyuan area are shown in Table 2. When considering different conditions, only one of the parameters is changed.

4.1. Cluster Spacing. The cluster spacing with 10 m, 15 m, 20 m, and 25 m was adopted to simulate the effect of it on the intercluster stress interference, in which the results are shown in Figure 8. And the minimum horizontal stress for the fractures shown in Figure 9 can fully reflect the intercluster stress interference.

A conclusion can be drawn from Figures 8–10 that the propagation of middle fracture is seriously interfered by stress when the cluster spacing is less than 15 m, so as the fracture is inhibited before it is up to the shale bedding plane. However, the cluster stress interference will be significantly weakened with the increasement of cluster spacing and the propagation morphology of multicluster fractures gradually tends to be more uniform. Consequently, the complicated fractures will be formed on the condition that the cluster spacing is between 15 m and 20 m in the light of the well-developed shale bedding plane.

4.2. Geological Condition

4.2.1. Horizontal Stress Difference. The utilization of the horizontal stress difference of 0 MPa, 2 MPa, 4 MPa, and

TABLE 4: Propagation behavior of the fractures at the shale bedding plane.

Shale bedding strength (MPa)	Open the bedding plane	Penetrate the shale bedding
0.5	Yes	No
2	Yes	Yes
4	No	Yes

6 MPa to investigate the influence of it on the propagation behavior of the fractures at the bedding plane and the simulation results are exhibited in Figure 11 and Table 3.

Figure 11 and Table 3 show that the length of middle fracture will be significantly decreased with the horizontal stress difference increasing from 0 MPa to 6 MPa. And the shear slip of bedding plane will be generated when the horizontal stress difference is lower than 2 MPa, which will conspicuously increase the stimulated reservoir volume, while the fractures will directly penetrate the shale bedding plane when the horizontal stress difference is higher than 2 MPa. However, the simulation results prove that the decrease of the minimum horizontal stress difference will give rise to the shear slip of bedding plane, but the propagation of the fractures in the direction of height is conspicuously inhibited.

4.2.2. Shale Bedding Strength. Keeping other factors constant, the shale bedding strength of 0.5 MPa, 2 MPa, and 4 MPa is used to investigate the effect of sophisticated interactive propagation of the fractures at the bedding plane, and the results are as follows.

It can be found from Figure 12 and Table 4 that the bedding plane will be initiated by the fractures and propagate along the plane when the strength of it is 0.5 MPa. And Figures 13 and 14 demonstrate the fractures will penetrate the shale bedding plane with the increasing of shale bedding strength from 0.5 MPa to 4 MPa, as well as the intercluster stress interference and the height of the fractures continuously rise. The simulation results suggest that the propagation of the fractures in the direction of length and height obviously increases when the strength of shale bedding plane is 2 MPa, which contribute the fractures to propagate widely to communicate with the bedding plane and consequently form the complex fractures.
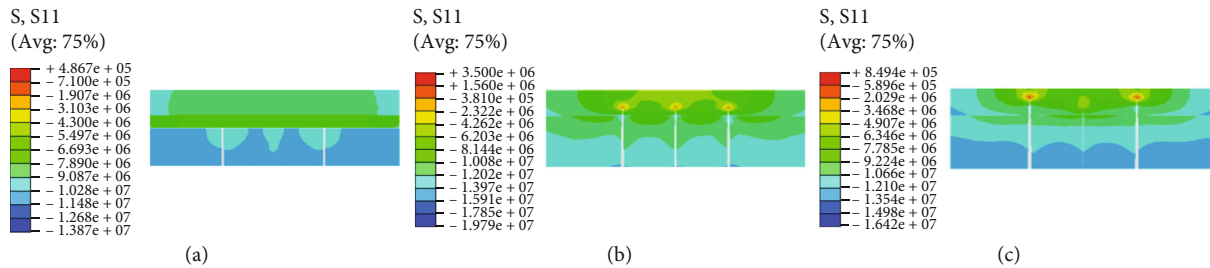
FIGURE 13: The cloud diagram of minimum horizontal stress of the fractures under different shale bedding strength: (a) 0.5 MPa, (b) 2 MPa, and (c) 4 MPa.
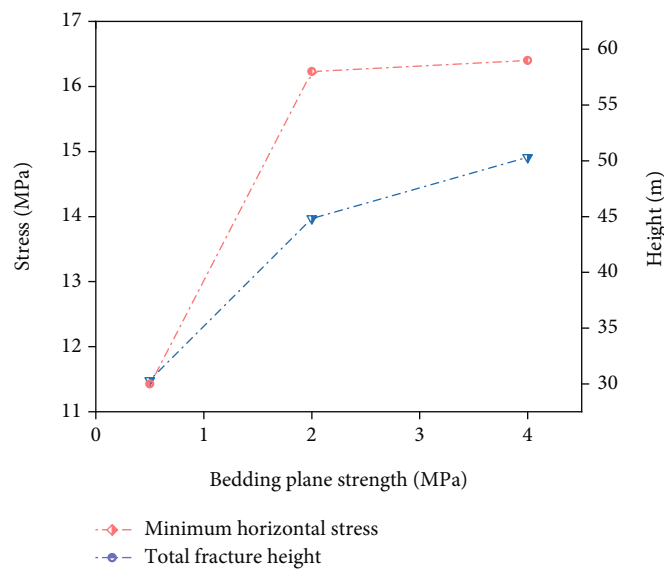

FIGURE 14: The fracture propagation data under different shale bedding strength.

4.3. Fracturing Construction Parameters

4.3.1. Perforation Density. Research the effect of perforation density on the dynamic distribution of fracturing fluid and the effective propagation among the fractures. Take the horizontal stress difference 6 MPa and the perforation density combination to 16-16-16, 16-18-16, and 16-20-16 which are simulated in Figure 15.

The length of the fracture in the middle markedly decreases with the horizontal stress difference increase. From Figures 15–17, the flow rate into the fractures increases with improving the density of perforation, counteracting the inhibition of intercluster stress interference on the propagation of the middle fracture, while the excessive difference of perforation density will evidently aggravate the uneven distribution of fluid. Therefore, the appropriate perforation density can be set in the field construction according to the distribution of reservoir bedding. And the density of perforation can be increased by 1-2 in the well-development bedding areas, which will comprehensively communicate bedding and form available complex fractures.

4.3.2. Injection Rate. Investigating the effect of injection rate on the propagation behavior of the fractures in the bedding plane, the injection rate of 11 m³/min, 12 m³/min, and 13 m³/min was calculated; see set in Figure 18.

Together given, the filtration of fracturing fluid remarkably reduces and the length of the fractures and the shear slip of the bedding plane gradually increase in Figure 18 with improvement of the injection rate. It can be seen from Figures 19 and 20 that the injection rate of fracturing fluid merely affects the morphology of the fractures and barely influences the intercluster stress interference. The simulation results prove that the fractures propagate widely to communicate with bedding plane and form complex fractures consequently when the injection rate is 12 m³/min, which will conspicuously increase the stimulated reservoir volume.

4.3.3. Fluid Viscosity. To illustrate the effect of viscosity on the propagation behavior of the fractures at the bedding plane, the viscosity of 1 mPa·s, 3 mPa·s, and 5 mPa·s was simulated and the results are as follows.

Figures 21–23 show that the width of each fracture changes significantly in correspondence with variation of viscosity, and with the increasing improvement of viscosity, the shear slip of the bedding plane is correspondingly going up more and more, but it has barely an effect on the propagation of the fractures in the length and height direction and
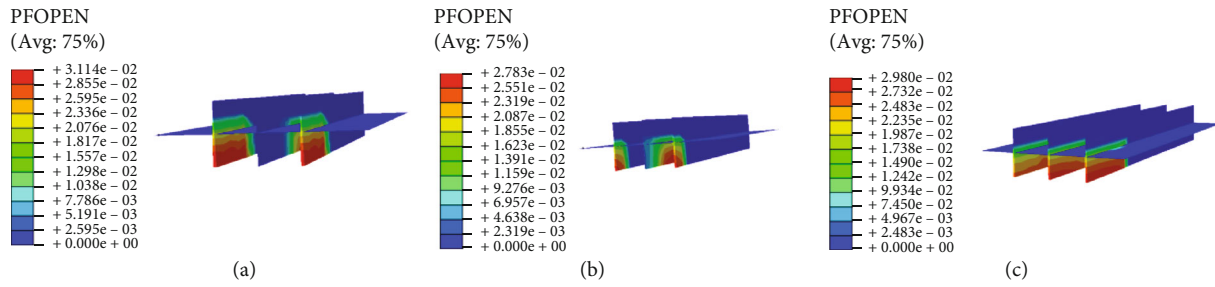
FIGURE 15: The propagation behavior of the fractures at the bedding plane under different perforation density: (a) 16-16-16, (b) 16-20-16, and (c) 16-18-16.
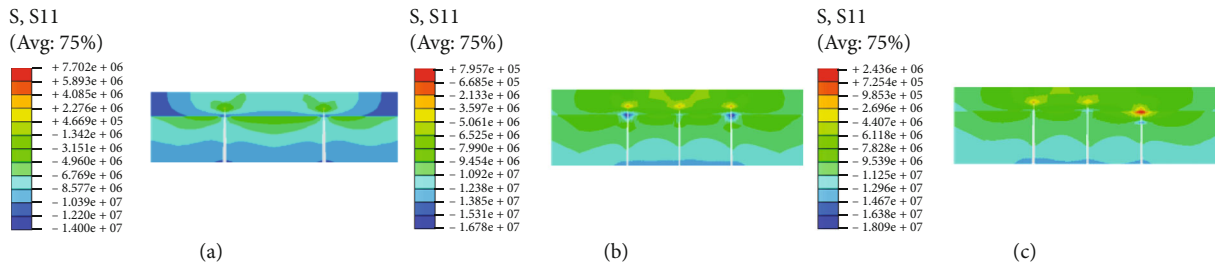

FIGURE 16: The cloud diagram of the minimum horizontal stress for the fractures under different perforation density: (a) 16-16-16, (b) 16-20-16, and (c) 16-18-16.
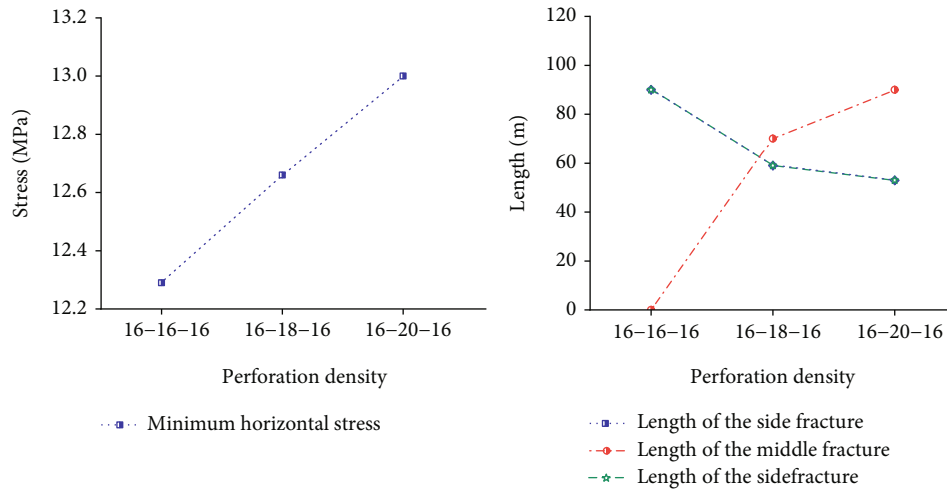

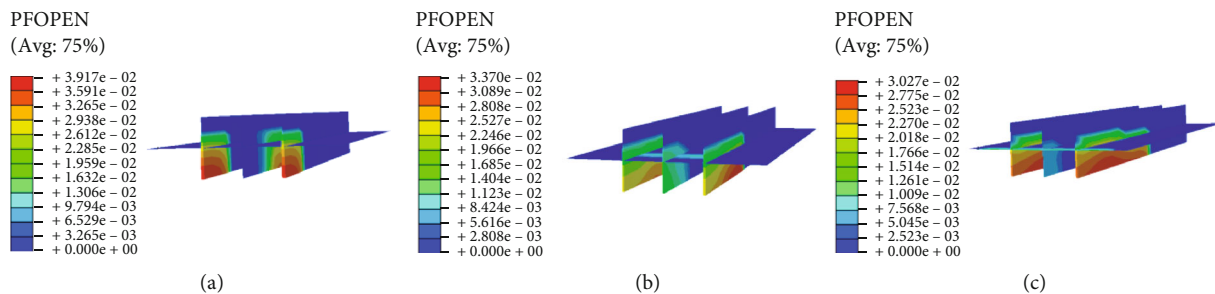FIGURE 17: The fracture propagation data under different perforation density.

FIGURE 18: The propagation behavior of the fractures at the bedding plane under different injection rates: (a) 11 m³/min, (b) 12 m³/min, and (c) 13 m³/min.

(a)   (b)   (c)
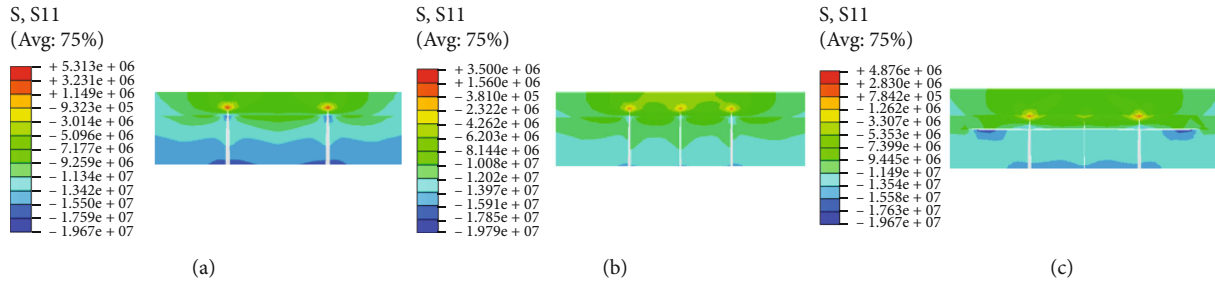
FIGURE 19: The cloud diagram of minimum horizontal stress for the fractures under different injection rates: (a) 11 m³/min, (b) 12 m³/min, and (c) 13 m³/min.
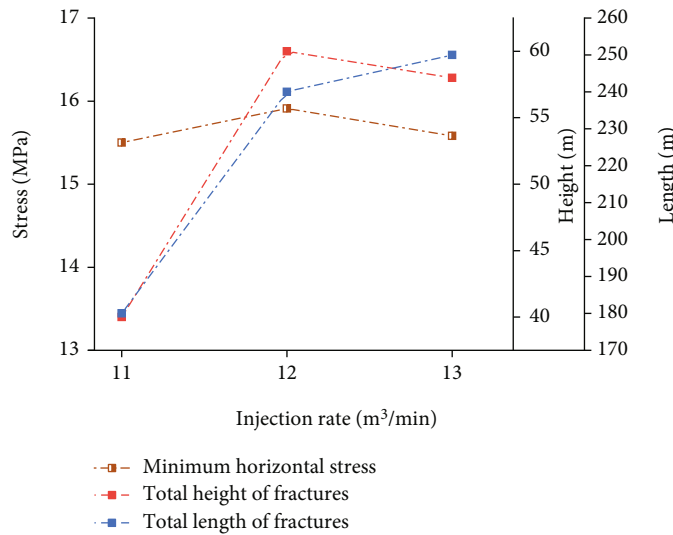

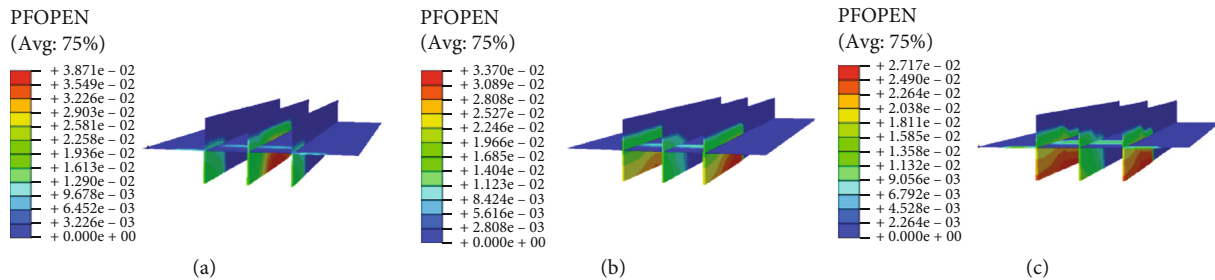FIGURE 20: The fracture propagation data under different injection rates.

(a)   (b)   (c)

FIGURE 21: The propagation behavior of the fractures at the bedding interface under different viscosity: (a) 1 mPa·s, (b) 3 mPa·s, and (c) 5 mPa·s.

(a)   (b)   (c)
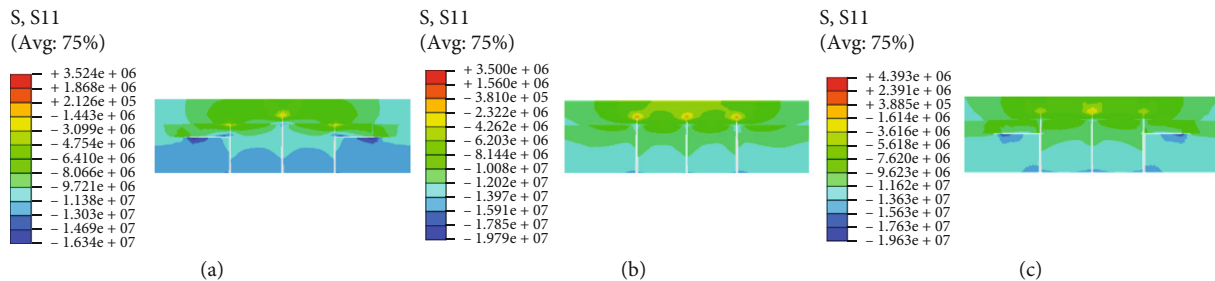
FIGURE 22: The cloud diagram of the minimum horizontal stress of fractures under different viscosity: (a) 1 mPa·s, (b) 3 mPa·s, and (c) 5 mPa·s.
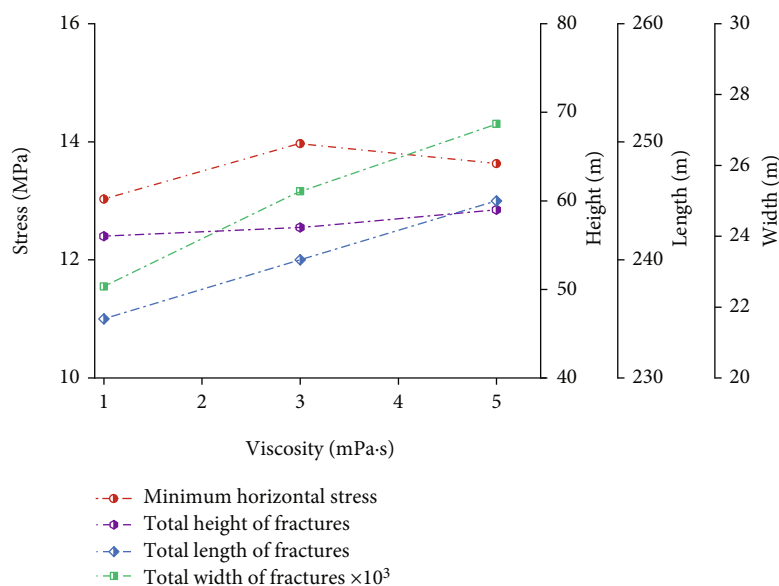
FIGURE 23: The fracture propagation data under different viscosity.

the intercluster stress interference, while the friction area will be extraordinarily obvious with increasing viscosity, which enormously influences the use of pumping pressure. The viscosity can be appropriately increased in areas with well-developed bedding, which will contribute to commendably increase the shear slip of the shale bedding plane and the stimulated reservoir volume.

5. Conclusions

A 3D finite element model of multicluster fracture propagation in bedded shale was established based on the cohesive zone model and the mechanism of the flow dynamic distribution for each cluster under the intercluster stress interference. And then, the propagation behavior of multicluster fractures at the bedding plane was revealed.

(1) Cluster spacing is one of the imperative factors affecting the intercluster stress interference, which will be correspondingly weakened on the condition that the value of cluster spacing is between 15 m and 20 m

(2) Horizontal stress difference and shale bedding strength are the indispensable factors affecting the sophisticated interactive propagation between the fractures and the bedding plane. Fractures will penetrate the shale bedding when the horizontal stress difference and shale bedding strength are over 4 MPa; conversely, the bedding plane will be opened and the shear slip is then generated. Meanwhile, in correspondence with the increase of them, the intercluster stress interference also increases conspicuously. Perforation density is one of the indispensable factors affecting the dynamic distribution of fracturing fluid among clusters; the perforation density of cluster in the middle can be increased by

1-2 compared to that of the bilateral cluster, which counteracts the inhibition of the intercluster stress interference on the propagation of the middle cluster

(3) In correspondence with the increase of injection rate and fluid viscosity, the shear slip of the bedding plane will increase prominently, and the friction will conspicuously increase with improvement of the viscosity. The high injection rate and viscosity fracturing fluid are conducive to the formation of complex fractures in areas with well-developed bedding

Data Availability

The data used to support the findings of this study are all shown in the uploaded manuscript.

Additional Points

Highlights. (1) The dynamic distribution of fracturing fluid flow during multicluster fracturing is considered in the theoretical model. (2) A 3D finite element model is established based on the cohesive zone model and the dynamic distribution mechanism of interfracture flow, and the cross-extensibility of multifractures and bedding interface is researched. (3) The propagation behavior of multifractures at the shale bedding plane considering intercluster stress interference is revealed.

Conflicts of Interest

The authors declare that there is no conflict of interest regarding the publication of this paper.

Acknowledgments

References

[1] Y. H. Wang, Y. Z. Liu, Y. H. Ding, L. F. Yang, Y. K. Zhang, and P. Tan, "Research on the influence of shale bedding to vertical extension mechanism of hydraulic fracture," *Drilling & Production Technology*, vol. 40, no. 5, pp. 39–42, 2017.

[2] S. Heng, C. H. Yang, Y. T. Guo, C. Y. Wang, and L. Wang, "Influence of shale beddings on hydraulic fracture propagation in shale formations," *Chinese Journal of Rock Mechanics and Engineering*, vol. 34, no. 2, pp. 228–237, 2015.

[3] A. R. Khoei, M. Vahab, and M. Hirmand, "Modeling the interaction between fluid-driven fracture and natural fault using an enriched-FEM technique," *International Journal of Fracture*, vol. 197, no. 1, pp. 1–24, 2016.

[4] G. Q. Zhang, D. W. Zhou, J. M. Dou, Y. X. Nie, and H. R. Dong, "Experiments on hydraulic fracture propagation under the action of natural fractures and crustal stress difference," *Journal of China University of Petroleum*, vol. 43, no. 5, pp. 157–162, 2019.

[5] P. Tan, Y. Jin, K. Han et al., "Analysis of hydraulic fracture initiation and vertical propagation behavior in laminated shale formation," *Fuel*, vol. 206, pp. 482–493, 2017.

[6] R. X. Zhang, B. Hou, H. F. Han, M. Fan, and M. Chen, "Experimental investigation on fracture morphology in laminated shale formation by hydraulic fracturing," *Journal of Petroleum Science and Engineering*, vol. 177, pp. 442–451, 2019.

[7] C. Bilgen, S. Homberger, and K. Weinberg, "Phase-field fracture simulations of the Brazilian splitting test," *International Journal of Fracture*, vol. 220, no. 1, pp. 85–98, 2019.

[8] B. Lei, J. P. Zuo, H. Y. Liu, J. T. Wang, F. Xu, and H. T. Li, "Experimental and numerical investigation on shale fracture behavior with different bedding properties," *Engineering Fracture Mechanics*, vol. 247, article 107639, 2021.

[9] J. B. Li, S. L. Wang, K. X. Dong, and X. Y. Zhao, "Dynamic distribution of multi-stage fracturing flow in horizontal well and optimization of fracture spacing," in *International Field Exploration and Development Conference*, pp. 2529–2550, Singapore, 2019.

[10] N. Sukumar, J. E. Dolbow, and N. Moës, "Extended finite element method in computational fracture mechanics: a retrospective examination," *International Journal of Fracture*, vol. 196, no. 1-2, pp. 189–206, 2015.

[11] T. Zhou, H. B. Wang, F. X. Li, Y. Z. Li, Y. S. Zou, and C. Zhang, "Numerical simulation of hydraulic fracture propagation in laminated shale reservoirs," *Petroleum Exploration and Development*, vol. 47, no. 5, pp. 1117–1130, 2020.

[12] T. Zhou, S. C. Zhang, Y. S. Zou, N. Li, and Y. H. Zheng, "Hydraulic fracture geometry of shale gas reservoirs with strong tectonic stress and large dip angle in Northeastern margin of Sichuan Basin," *Xinjiang Petroleum Geology*, vol. 37, no. 3, pp. 336–341, 2016.

[13] Y. Liu, H. Q. Yang, Q. Q. Zhang, and D. Xiong, "Properties of a shale bedding plane and its influence on the geometric parameters of fracture propagation in volume fracturing," *Engineering Fracture Mechanics, article*, vol. 266, article 108413, 2022.

[14] W. J. Xu, Y. M. Li, J. Z. Zhao, X. Y. Chen, and Y. Peng, "Formation mechanism of complex fracture network under horizontal fracturing in shale gas reservoir," *Reservoir evaluation and development*, vol. 7, no. 5, pp. 64–73, 2017.

[15] K. Wu and J. E. Olson, "A simplified three-dimensional displacement discontinuity method for multiple fracture simula-tions," *International Journal of Fracture*, vol. 193, no. 2, pp. 191–204, 2015.

[16] Y. Z. Wang, B. Hou, D. Wang, and Z. H. Jia, "Features of fracture height propagation in cross-layer fracturing of shale oil reservoirs," *Petroleum Exploration and Development*, vol. 48, no. 2, pp. 469–479, 2021.

[17] S. Ji, J. H. Zhang, C. Y. Zhang, T. T. Jiang, and G. Huang, "Numerical model on predicting hydraulic fracture propagation in low-permeability sandstone," *International Journal of Damage Mechanics*, vol. 30, no. 2, pp. 297–320, 2021.

[18] Y. L. Zhang, B. Han, X. Zhang, Y. Jia, and C. Zhu, "Study of interactions between induced and natural fracture effects on hydraulic fracture propagation using a discrete approach," *Lithosphere*, vol. 2021, no. Special 4, 2021.

[19] C. Sun, H. Zheng, W. D. Liu, and W. T. Lu, "Numerical simulation analysis of vertical propagation of hydraulic fracture in bedding plane," *Engineering Fracture Mechanics*, vol. 232, article 107056, 2020.

[20] S. Suo, J. Zhang, F. P. Feng, J. Z. Ji, Q. Y. Ye, and L. H. Yang, "Study on the evolution law of shale hydraulic fracture interacting with bedding layer under pulsation loading," *Lithosphere*, vol. 2022, no. Special 4, 2022.

[21] D. Xiong, X. F. Ma, H. Q. Yang, Y. Liu, and Q. Q. Zhang, "Experimental and numerical simulation of interlayer propagation path of vertical fractures in shale," *Frontiers in Energy Research*, vol. 9, 2021.

[22] X. Q. Liu, Z. Q. Qu, T. K. Guo, Y. Sun, Z. Y. Wang, and B. H. Elham, "Numerical simulation of non-planar fracture propagation in multi-cluster fracturing with natural fractures based on lattice methods," *Engineering Fracture Mechanics*, vol. 220, article 106625, 2019.

[23] Y. Li, J. G. Deng, W. Liu et al., "Numerical simulation of limited-entry multi-cluster fracturing in horizontal well," *Journal of Petroleum Science and Engineering*, vol. 152, pp. 443–455, 2017.

[24] Y. Li, J. G. Deng, W. Liu, W. Yan, W. K. Cao, and P. F. Wang, "Numerical simulation of limited entry technique in multistage and multi-cluster horizontal well fracturing," *Fault-Block oil & Gas Field*, vol. 24, no. 1, pp. 69–73, 2017.

[25] J. Z. Zhao, X. Y. Chen, Y. M. Li, B. Fu, and W. J. Xu, "Numerical simulation of multi-stage fracturing and optimization of perforation in a horizontal well," *Petroleum Exploration and Development*, vol. 44, no. 1, pp. 119–126, 2017.

[26] L. H. Pan, S. C. Zhang, L. J. Cheng, C. H. Lu, and K. Y. Liu, "A numerical simulation of the inter-cluster interference in multi-cluster staged fracking for horizontal wells," *Natural Gas Industry*, vol. 34, no. 1, pp. 74–79, 2014.

[27] C. Zienkiewicz and R. L. Taylor, *The Finite Element Method for Solid and Structural Mechanics*, Elsevier, 2005.

[28] P. C. Dong and X. H. Xu, "Numerical simulation of water-flooding for heterogeneous oil reservoir in lamina scale acta," *Acta Petrolei Sinica*, vol. 19, no. 1, pp. 64–70, 1998.

[29] J. L. Elbel, A. R. Piggott, and M. G. Mack, "Numerical modeling of multilayer fracture treatments," in *Presented at the SPE Permian Basin Oil and Gas Recovery Conference One Petro*, pp. 16–20, Midland, Texas, 1992.

[30] J. B. Crump and M. W. Conway, "Effects of perforation-entry friction on bottomhole treating analysis," *Journal of Petroleum Technology*, vol. 40, no. 8, pp. 1041–1048, 1988.

[31] Z. Chen, R. G. Jeffrey, and X. Zhang, "Numerical modeling of three-dimensional T-shaped hydraulic fractures in coal seams

using a cohesive zone finite element model," *Hydraulic Fracturing Journal*, vol. 2, no. 2, pp. 20–37, 2015.

[32] Z. Chen, R. G. Jeffrey, X. Zhang, and J. Kear, "Finite element simulation of a hydraulic fracture interacting with a natural fracture," *SPE Journal*, vol. 22, no. 1, pp. 219–234, 2017.

[33] J. Adachi, E. Siebrits, A. Peirce, and J. Desroches, "Computer simulation of hydraulic fractures," *International Journal of Rock Mechanics and Mining Sciences*, vol. 44, no. 5, pp. 739–757, 2007.

[34] S. L. Liu, S. X. Chen, F. Yu, and W. G. Zhao, "Anisotropic properties study of chlorite schist," *Rock and Soil Mechanics*, vol. 33, no. 12, pp. 3616–3623, 2012.

[35] J. W. Cho, H. Kim, S. Jeon, and K. B. Min, "An experimental study on deformation and strength anisotropy of transversely isotropic rocks in Korea," in *ISRM Congress, OnePetro*, pp. 293-294, Taylor & Francis Group, London, 2011.